Medical Image Analysis 53 (2019) 179–196

Contents lists available at ScienceDirect

Medical Image Analysis

journal homepage: www.elsevier.com/locate/media

Frequency-splitting dynamic MRI reconstruction using multi-scale 3D convolutional sparse coding and automatic parameter selection ☆

Thanh Nguyen-Duc, Tran Minh Quan, Won-Ki Jeong*

School of Electrical and Computer Engineering, Ulsan National Institute of Science and Technology (UNIST), South Korea

ARTICLE INFO

Article history:
Received 7 March 2018
Revised 8 December 2018
Accepted 1 February 2019
Available online 7 February 2019

Keywords:
Compressed sensing
Dynamic MRI
Parallel MRI
Image reconstruction
Frequency filter
Multi-scale 3D convolutional sparse coding
Elastic net regularization
Total variation
Genetic algorithm
GPU

ABSTRACT

In this paper, we propose a novel image reconstruction algorithm using multi-scale 3D convolutional sparse coding and a spectral decomposition technique for highly undersampled dynamic Magnetic Resonance Imaging (MRI) data. The proposed method recovers high-frequency information using a shared 3D convolution-based dictionary built progressively during the reconstruction process in an unsupervised manner, while low-frequency information is recovered using a total variation-based energy minimization method that leverages temporal coherence in dynamic MRI. Additionally, the proposed 3D dictionary is built across three different scales to more efficiently adapt to various feature sizes, and elastic net regularization is employed to promote a better approximation to the sparse input data. We also propose an automatic parameter selection technique based on a genetic algorithm to find optimal parameters for our numerical solver which is a variant of the alternating direction method of multipliers (ADMM). We demonstrate the performance of our method by comparing it with state-of-the-art methods on 15 single-coil cardiac, 7 single-coil DCE, and a multi-coil brain MRI datasets at different sampling rates (12.5%, 25% and 50%). The results show that our method significantly outperforms the other state-of-the-art methods in reconstruction quality with a comparable running time and is resilient to noise.

1. Introduction

Dynamic magnetic resonance imaging (MRI), including dynamic contrast-enhanced (DCE) MRI and cardiac MRI, has been widely used to analyze changes in tissue characteristics or the movement of organs over time. Since dynamic MRI's diagnostic performance is highly correlated with its temporal resolution (El Khouli et al., 2009), speeding up the acquisition time has been actively studied in the recent decades. More recently, compressed sensing theory (Donoho, 2006) has been applied to the MRI reconstruction problem (Lustig et al., 2008) to reduce the acquisition time. The objective of CS-MRI is to achieve close-to-perfect reconstruction from sub-Nyquist sampling (Shannon, 1949) of k-space data from the MRI scanner. Otazo et al. (2012) showed that the computational approach to CS-MRI can also accelerate conventional imaging. Slow numerical computation of CS-MRI reconstruction process can be further accelerated by leveraging parallel computing hardware such as graphics processing units (GPUs) (Quan et al., 2015).

Early work on CS-MRI exploited the sparsity of signal by applying universal sparsifying transforms such as the Fourier transform, total variation (TV) (Ma et al., 2008), and Wavelets (Daubechies, 1992). For dynamic CS-MRI, spatio-temporal correlations are commonly used (e.g., $k-t$ FOCUSS (Jung et al., 2007, 2009)). Dictionary learning, a technique extracting common feature sets (i.e. atoms) from the training data, has been employed in CS-MRI to replace universal sparsifying transforms (Ravishankar and Bresler, 2011; Awate and DiBella, 2012; Lingala and Jacob, 2013; Caballero et al., 2012, 2014). Since dictionary learning can generate custom-designed atoms that are better fit to the target image, reconstruction quality improves significantly compared to that of universal transforms. Recently, a filter-based dictionary learning method such as convolutional sparse coding (CSC) (Bristow et al., 2013; Wohlberg, 2014), has been proposed to overcome the drawbacks of conventional patch-based dictionary learning, which includes generating redundant atoms and longer running time. CSC has been successfully adopted in solving dynamic CS-MRI problems (Quan and Jeong, 2016a, 2016b).

In this paper, we introduce a novel dynamic CS-MRI reconstruction method that extends state-of-the-art CSC-based reconstruction methods (Quan and Jeong, 2016a, 2016b). First, we employ frequency filtering to separate low- and high-frequency components of the target image, and then use a relatively simple energy min-

☆ **Conflict of Interest:** None.

* Corresponding author.
E-mail addresses: thanhnguyencsbk@unist.ac.kr (T. Nguyen-Duc), quantm@unist.ac.kr (T.M. Quan), wkjeong@unist.ac.kr (W.-K. Jeong).

https://doi.org/10.1016/j.media.2019.02.001
1361-8415/

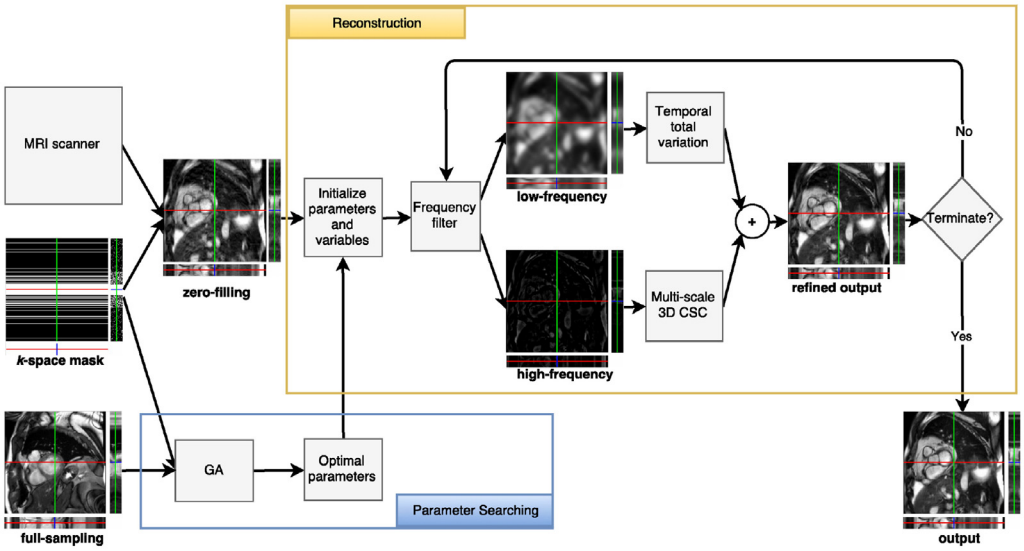

Fig. 1. Overview of the proposed CS-MRI reconstruction process based on multi-scale 3D CSC with spectral decomposition and optimal parameter selection using a genetic algorithm.

imization process based on a temporal total variation (TV) energy for low-frequency reconstruction while more expensive feature encoding resources (i.e. dictionary of convolutional filters) are dedicated only to recovering high-frequency component of the image (see Fig. 1 for the overview of the reconstruction process). The motivation behind this approach is that, in conventional CS-MRI, low-frequency k-space data is more densely sampled (see Fig. 4c k-space mask) while filter-based dictionary learning can better represent sparse local features in high-frequency data. Second, we employ 3D convolutional filters in various scales and elastic net regularization (Zou and Hastie, 2005) to further improve the reconstruction quality compared to conventional approaches that only use a single-scale dictionary and l_1 regularization (Caballero et al., 2014; Quan and Jeong, 2016a). Third, we propose an automatic optimal parameter-selection method based on a genetic algorithm (GA) for our iterative numerical solver, which is a variant of the alternating direction method of multipliers (ADMM). The proposed GA method belongs to the class of metaheuristics algorithms (Luke, 2009) inspired by natural evolution to optimize objective function (Mühlenbein et al., 1991). Our approach uses a GA only once to automatically find a set of optimal parameters without manual intervention, and then we can reuse them to reconstruct similar datasets. In our experiment on 15 cardiac and 7 dynamic contrast-enhanced (DCE) MRI datasets in three different Cartesian sampling rates (12.5%, 25% and 50%), the proposed reconstruction method produces significantly better image quality, compared to several state-of-the-art methods (e.g., $k-t$ FOCUSS (Jung et al., 2007, 2009)), single-scale 3D CSC (Quan and Jeong, 2016a), blind compressive sensing (Lingala and Jacob, 2013), patch-based dictionary learning (Caballero et al., 2012, 2014), and FTVNNR (Yao et al., 2018), and runs at an efficient rate with GPU acceleration.

The rest of the paper is organized as follows. Section 2 reviews the recent literature related to the proposed method. Details of the proposed reconstruction process and its computational complexity analysis are given in Section 3. We demonstrate the performance of our reconstruction method and compare it with state-of-the-art methods in Section 4. Finally, we summarize our work and propose future research directions in Section 5.

2. Related work

Since its inception in Lustig et al. (2008)'s seminal work, CS-MRI has been actively studied to accelerate the time-consuming MRI imaging process. Conventional CS-MRI algorithms are mainly based on promoting sparsity in the data by employing l_1 regularization in universal sparsifying transformation models. In such methods, the target image is transformed into a sparse domain by applying universal transforms such as Wavelet and Fourier transforms or total variation operation (Lustig et al., 2006; Montefusco et al., 2011). CS-MRI for dynamic data is also proposed by enforcing spatial and temporal coherence (i.e., $k-t$ FOCUSS (Jung et al., 2007, 2009) and Chen et al. (2016)). These conventional CS-MRI methods suffer from computational overhead because of solving expensive nonlinear l_1 minimization problems. This leads to the development of efficient numerical algorithms (Goldstein and Osher, 2009; Boyd et al., 2011) that leverage the Alternating Direction Method of Multipliers (ADMMs) to solve this nonlinear problem in CS-MRI (Quan et al., 2015). CS-MRI reconstruction methods using nuclear norm and low-rank matrix completion techniques (Trémoulhéac et al., 2014; Miao et al., 2015; Yao et al., 2015, 2018; Ravishankar et al., 2017; Zhu et al., 2018) have also been proposed.

More recently, while the major limitation of universal transform-based methods is just using transformation in general, dictionary learning (DL) (Aharon et al., 2006), an unsupervised learning approach, can be adapted to features from input data by training dictionary. Thus, conventional DL in CS-MRI (Ravishankar and Bresler, 2011; Awate and DiBella, 2012; Lingala and Jacob, 2013; Caballero et al., 2012, 2014) approaches have successfully applied to enhancing MRI reconstruction quality. Caballero et al. (Caballero et al., 2012, 2014), for instance, demonstrated the efficiency of using patch-based DL for dynamic MRI reconstruction with temporal TV filter for enforcing coherence of time-axis. Efficient convolutional sparse coding (CSC) is then introduced by minimizing an energy objective function using a convolutional operator on the image domain, which leads to element-wise in the frequency domain, derived within ADMMs framework (Bristow et al., 2013; Wohlberg, 2014, 2016). Quan and Jeong (2016a,b) first employed CSC to solve CS-MRI problems, which significantly improves running time and reconstruction quality by building more compact and expressive shift-invariance con-

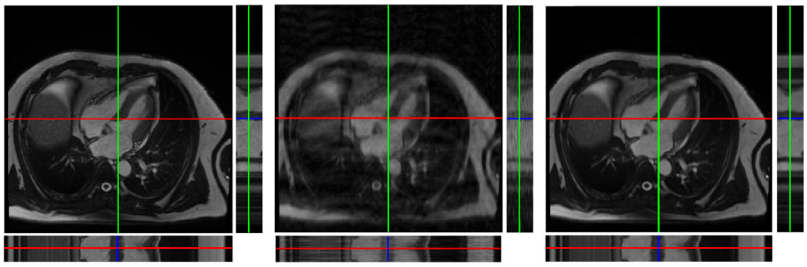

(a) Full-sampling (b) Zero-filling (c) Converged result

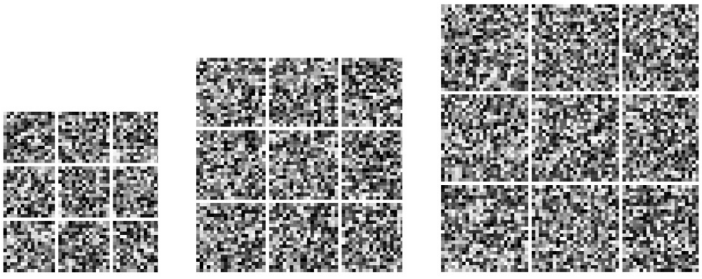

(d) Initial filters

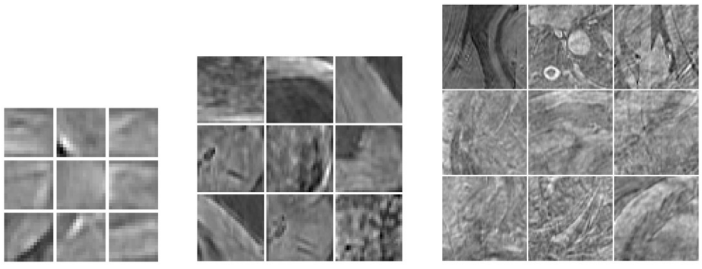

(e) 2D view of converged filters

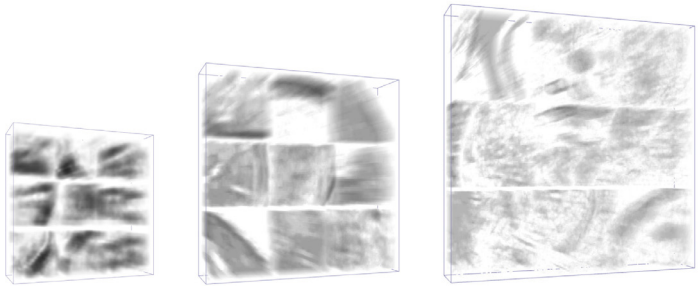

(f) 3D view of converged filters

Fig. 2. Overview multi-scale 3D CSC for CS-MRI reconstruction.

volutional filters. Nevertheless, MR data contains various feature sizes so that multiple dictionary sizes in the multi-scale 3D CSC method can adapt well to the data rather than single-scale atom size methods (e.g., (Lingala and Jacob, 2013; Caballero et al., 2014; Quan and Jeong, 2016a)). The multi-scale 3D CSC in our method builds the dictionary by simultaneously learning shift-invariant multiple sizes of convolutional filters from data (Fig. 2). In this approach, zero-filling (Fig. 2b, zero-filling reconstruction) and randomly initialized filters (e.g., in Fig. 2d, the various filter sizes) are updated iteratively until they converge, as shown in Fig. 2c, e, and f.

There are a few approaches that leverage different reconstruction strategies based on the frequency range of the image. Yang et al. (2015) proposed a two-stage reconstruction method which performs the first-step reconstruction of low-frequency component only from the central region of *k*-space data, and then combines this result with the remaining *k*-space data (corresponding to high-frequency component) to conduct the second-step reconstruction from the full *k*-space data. A filter-based reconstruction approach (Wu et al., 2016) separates *k*-space with high- and low-pass filters, reconstructs each frequency component independently, and combines the reconstructed results to generate the fi-

nal image. Our method shares a similar idea with these previous work by splitting k-space (i.e. frequency) data, but our method employs advanced reconstruction methods specifically designed to leverage characteristics of each frequency (i.e. multi-scale 3D CSC for sparsity in high-frequency and temporal TV for coherency in low-frequency). Furthermore, our method iteratively updates the result to enforce the measurement consistency (see Algorithm 1

Algorithm 1 Iterative reconstruction process using spectral decomposition.

procedure RECONSTRUCTION(m) ▷ m: sparse measurement of k-space
  $s \leftarrow \mathcal{F}_2^H(m)$ ▷ input: zero-filling reconstruction
  while stopping criteria not met **do**
    $s^l = \mathcal{F}_2^H H \mathcal{F}_2(s)$ ▷ H: low-pass filter; $\mathcal{F}_2$: 2D Fourier transform
    $s^h = s - s^l$
    Solve for s^l using temporal TV ▷ Eq. 5
    Solve for s^h using multi-scale 3D CSC ▷ Eq. 9
    $s \leftarrow s^l + s^h$
  return s ▷ s with removed artifact

and the constrain term in Eq. (4)) while the other methods perform one-time reconstruction for each frequency data and then combining them.

Genetic algorithm (GA) is a population-based method which is inspired by nature's capability to evolve living beings well-adapted to their environment (Blum and Roli, 2003; Luke, 2009). This meta-heuristic algorithm, which is well known in optimization problem with many applications (Mühlenbein et al., 1991; Blum and Roli, 2003; Luke, 2009), deals in every iteration with a set of solutions rather than with a single solution (i.e. hill-climbing, simulated annealing and tabu search). The main idea of GA is generating a sequence of populations (i.e. generations) where each individual in a population is a solution to the problem. A new generation is created from the previous generation using natural operations such as mutations and crossovers based on the fitness values from members of the current population. This evolution process stops when the number of generations is greater than the pre-defined number and outputs an individual which has a minimum fitness value. Meta-heuristics in optimization is an immense research field and many different classes of algorithms exist, such as single-state methods, population methods, and hybrid methods (Blum and Roli, 2003; Luke, 2009). To the best of our knowledge, our approach is the first attempt to use GA for automatic parameter selection in the CS-MRI reconstruction problem.

This paper extends our previous work (Quan and Jeong, 2016a; Nguyen-Duc and Jeong, 2018) with significant improvements and differences. In this paper, we significantly improve the reconstructed image quality by splitting the image into high- and low-frequency components and apply different reconstruction strategies, i.e., low-frequency component is reconstructed using a conventional energy minimization method enforcing temporal coherency while high-frequency component is reconstructed using a 3D CSC method. In addition, we newly introduce an automatic parameter optimization method using a GA. We also show how the proposed method can be applied to parallel MRI data. More rigorous performance validation on 22 real dynamic MRI datasets in various sampling rates and noise levels, compared with state-of-the-art methods, are presented in this paper, which was not provided in the previous work.

3. Method

The overview of our proposed CS-MRI reconstruction process is illustrated in Fig. 1. The input to our method is a zero-filling reconstruction that is generated by applying inverse Fourier transform to the undersampled k-space data from the MRI scanner, which suffers from undersampling artifacts. Then, the proposed method consists of two components: *the reconstruction process* that takes a zero-filling reconstruction as an initial guess to improve image quality (i.e. removing undersampling artifact, Fig. 1 yellow box), and *the parameter searching process* using a GA (Fig. 1 blue box).

3.1. Reconstruction process

In the reconstruction process, the input zero-filling reconstruction image is separated into low- and high-frequency zero-filling images by applying a band-pass frequency filter. The high-frequency image is then reconstructed by using multi-scale 3D CSC with elastic net regularization. This multi-scale CSC method adapts well to features of various sizes, and elastic net regularization can outperform l_1-only regularization without impairing the sparsity of representation (Zou and Hastie, 2005). In the meantime, the low-frequency image is reconstructed by minimizing the total variation along the temporal direction (i.e., promoting sparsity in the temporal gradient field), which is based on the observation that the information in dynamic MRI data is sparser in first-order temporal gradients than in spatial gradients (Caballero et al., 2014). At the end of the reconstruction process, the reconstructed low- and high-frequency images are combined together to generate a refined output (i.e. undersampling artifact is reduced). This update process is repeated (see Algorithm 1) until reaching the stopping criteria in which the number of iterations are greater than a pre-defined number, or primal and dual residuals are less than an absolute value, as discussed in Sec. 3.3 of (Boyd et al., 2011). More detailed discussions of the proposed method are presented in the following sections.

3.1.1. Spectral decomposition using a frequency filter

To apply different reconstruction strategies based on the frequency range, we decompose the input image into low- and high-frequency images by applying a two-dimensional Butterworth low-pass filter (BLPF) to every 2D MRI slice in the frequency domain. The transfer function $H(u, v)$ of the BLPF of order n with a cutoff frequency at a specified distance D_0 from the origin is defined as follows:

$$H(u,v) = \frac{1}{1 + [D(u,v)/D_0]^{2n}} \tag{1}$$

where $D(u, v)$ is the distance from a point (u, v) to the center of the frequency domain, and the parameters D_0 and n define how the frequency is cut off. Thus, for the input image s, the low-frequency image s^l can be computed using two-dimensional Fourier transform $\mathcal{F}_2$ and its inverse $\mathcal{F}_2^H$ along the time-axis as follows:

$$s^l = \mathcal{F}_2^H H \mathcal{F}_2(s) \tag{2}$$

and the high-frequency image s^h can be computed as follows:

$$s^h = s - s^l \tag{3}$$

The choice of D_0 and n can be automatically made via our proposed parameter selection method (see Section 3.2).

3.1.2. Temporal total variation and multi-scale 3D CSC for reconstruction

After the frequency filter splits the input image s into high (s^h) and low (s^l) frequency images, the reconstruction process reduces

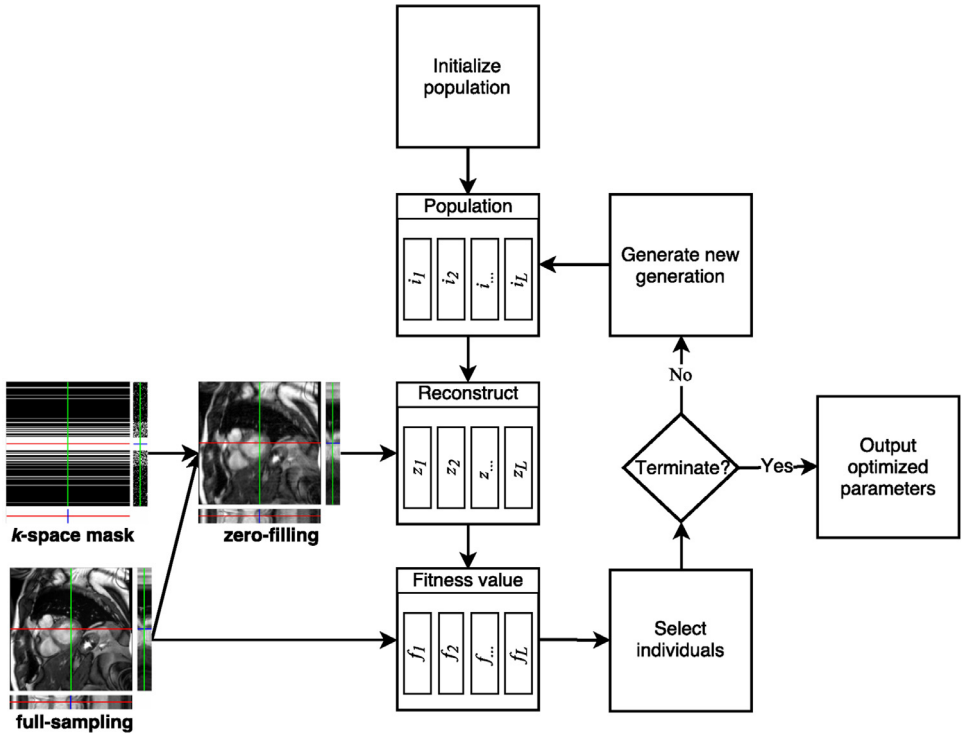

Fig. 3. Genetic algorithm for automatically searching optimal parameters.

undersampling artifact in s by solving the energy minimization problem as follows:

$$\min_{d,x,s^h,s^l} \frac{\alpha}{2}\left\|s^h - \sum_n^N \sum_k^K d_{n,k} * x_{n,k}\right\|_2^2 + \lambda_1 \sum_n^N \sum_k^K \left\|x_{n,k}\right\|_1 + \frac{\lambda_2}{2} \sum_n^N \sum_k^K \left\|x_{n,k}\right\|_2^2 + \theta \left\|\nabla_t s^l\right\|_1$$
$$s.t.: \|R\mathcal{F}_2(s^h + s^l) - m\|_2^2 < \epsilon^2, \|d_{n,k}\|_2^2 \le 1 \quad (4)$$

where N is the number of filter scales (i.e. levels), K is the number of filters in each scale, $*$ is a convolution operator, $d_{n,k}$ is the k-th filter (or atom) in n^{th} dictionary (i.e. dictionary for level n), and $x_{n,k}$ is its corresponding sparse code (or sparse map) for s^h. Note that the dimension of the filters we used were $15 \times 15 \times 20$, $20 \times 20 \times 25$, and $25 \times 25 \times 30$, and the dimension of the sparse map $x_{n,k}$ was identical to the size of the image. In Eq. (4), the first term measures the difference between s^h and its sparse approximation $s^h - \sum\sum d_{n,k} * x_{n,k}$, weighted by α. The combination of the second and third terms, which are weighted by λ_1 and λ_2 parameters, are called elastic net regularization (Zou and Hastie, 2005). The fourth term $\theta\|\nabla_t s^l\|_1$ is the total variation energy that enforces the temporal coherence of the low-frequency image. The rest of this equation is the collection of constraints: the first constraint keeps the consistency between undersampled measurement m and the undersampled reconstructed image using k-space mask R with $\mathcal{F}_2$ operator; the second constraint restricts the Frobenius norm of each atom $d_{n,k}$ within a unit length. In following discussion, we simplify the notations without indices n, k and also replace the result of Fourier transform of a given variable by using subscript f (for instance, d_{f_3} represents simplified notation for $\mathcal{F}_3 d$ in the 3D domain and $s^h_{f_2}$ is the simplified notation for $\mathcal{F}_2 s^h$ in the 2D spatial domain). The problem (4) can be split into two sub-optimization problems as follows, which can be iteratively updated for the global minimum solution.

Temporal TV minimization: we minimize Eq. (4) with respect to s^l, which contains the total variation along the time-axis and the measurement constraint term.

$$\min_{s^l} \ \theta\|\nabla_t s^l\|_1 \quad s.t.: \|R\mathcal{F}_2(s^h + s^l) - m\|_2^2 < \epsilon^2 \quad (5)$$

Eq. 5 can be written in an unconstrained form with γ parameter, as shown in Eq. (6) below:

$$\min_{s^l} \ \theta\|\nabla_t s^l\|_1 + \frac{\gamma}{2}\|R\mathcal{F}_2(s^h + s^l) - m\|_2^2 \quad (6)$$

This problem can be efficiently solved by an iterative clipping algorithm using the primal-dual method (Chambolle, 2005).

$$s^l_{(i+1)} = \frac{\gamma}{2}\mathcal{F}_2^H m^l - \nabla_t^T z_{(i)}$$
$$z_{(i+1)} = clip\left(z_{(i)} + \frac{1}{\eta}\nabla_t s^l_{(i+1)}, \frac{\theta}{2}\right) \quad (7)$$

where m^l is equal to $m - R\mathcal{F}_2 s^h$ and i is the iteration number. The clipping function is defined in Eq. (8).

$$clip(a,b) = \begin{cases} a, & \text{if } |a| \le b \\ b \cdot sign(a), & \text{if } |a| \ge b \end{cases} \quad (8)$$

The index i starts with 0, the initial $z_{(0)} = 0$, and $\eta \ge maxeig(\nabla_t \nabla_t^T)$. In this case, the maximum eigenvalue of $\nabla_t \nabla_t^T$ is less than four regardless to the length of signal; thus, we can set $\eta = 4$ and the maximum number of iterations equals 40 in our experiments. Note that θ and γ are optimized by using a GA (see Section 3.2). For more details on parameter and derivation about the algorithm, refer to Chambolle (2005).

Multi-scale 3D CSC with elastic net regularization: In this problem, we find s^h in the energy minimization function, as follows:

$$\min_{d,x,s^h} \frac{\alpha}{2}\left\|s^h - \sum_n^N \sum_k^K d_{n,k} * x_{n,k}\right\|_2^2$$

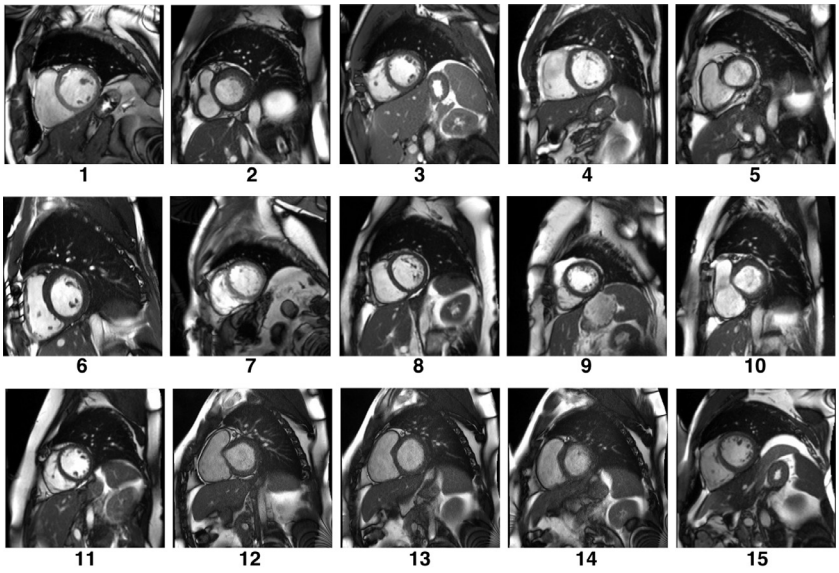

(a) Cardiac datasets

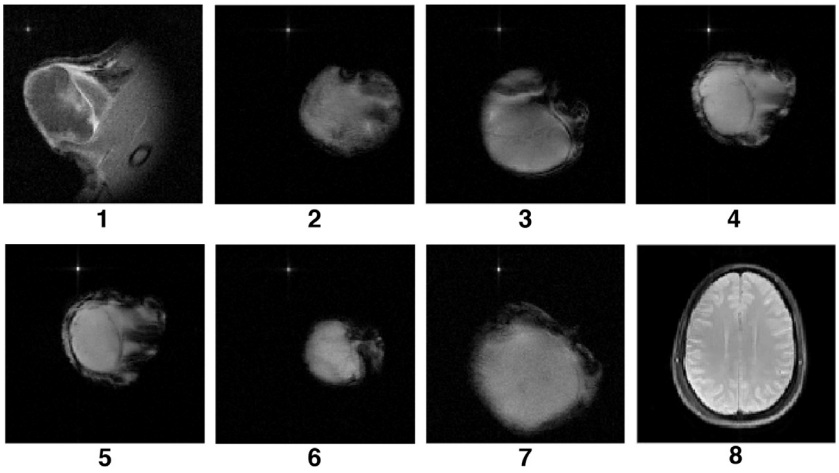

(b) Tumor DCE (1-7) and multi-coil brain (8) datasets

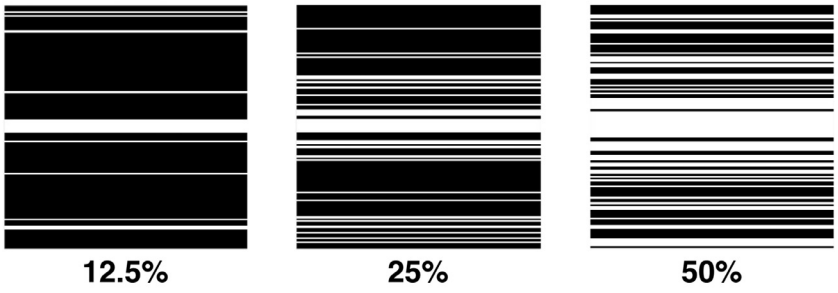

(c) Undersampling k-space masks

Fig. 4. MRI datasets and Cartesian undersampling masks used in our experiments.

$$+ \lambda_1 \sum_{n}^{N} \sum_{k}^{K} \left\| x_{n,k} \right\|_1 + \frac{\lambda_2}{2} \sum_{n}^{N} \sum_{k}^{K} \left\| x_{n,k} \right\|_2^2$$
$$s.t. : \|R\mathcal{F}_2(s^h + s^l) - m\|_2^2 \ < \ \epsilon^2, \|d_{n,k}\|_2^2 \leq 1 \tag{9}$$

Eq. (9) can be re-written using auxiliary variables y and g for x and d, as follows:

$$\min_{d,x,g,y,s^h} \frac{\alpha}{2} \left\| s^h - \sum\sum d * x \right\|_2^2 + \lambda_1 \|y\|_1 + \frac{\lambda_2}{2} \|y\|_2^2$$
$$s.t. : x - y = 0, \|R\mathcal{F}_2 s^h - m^h\|_2^2 \ < \ \epsilon^2,$$
$$g = Proj(d), \|g\|_2^2 \leq 1 \tag{10}$$

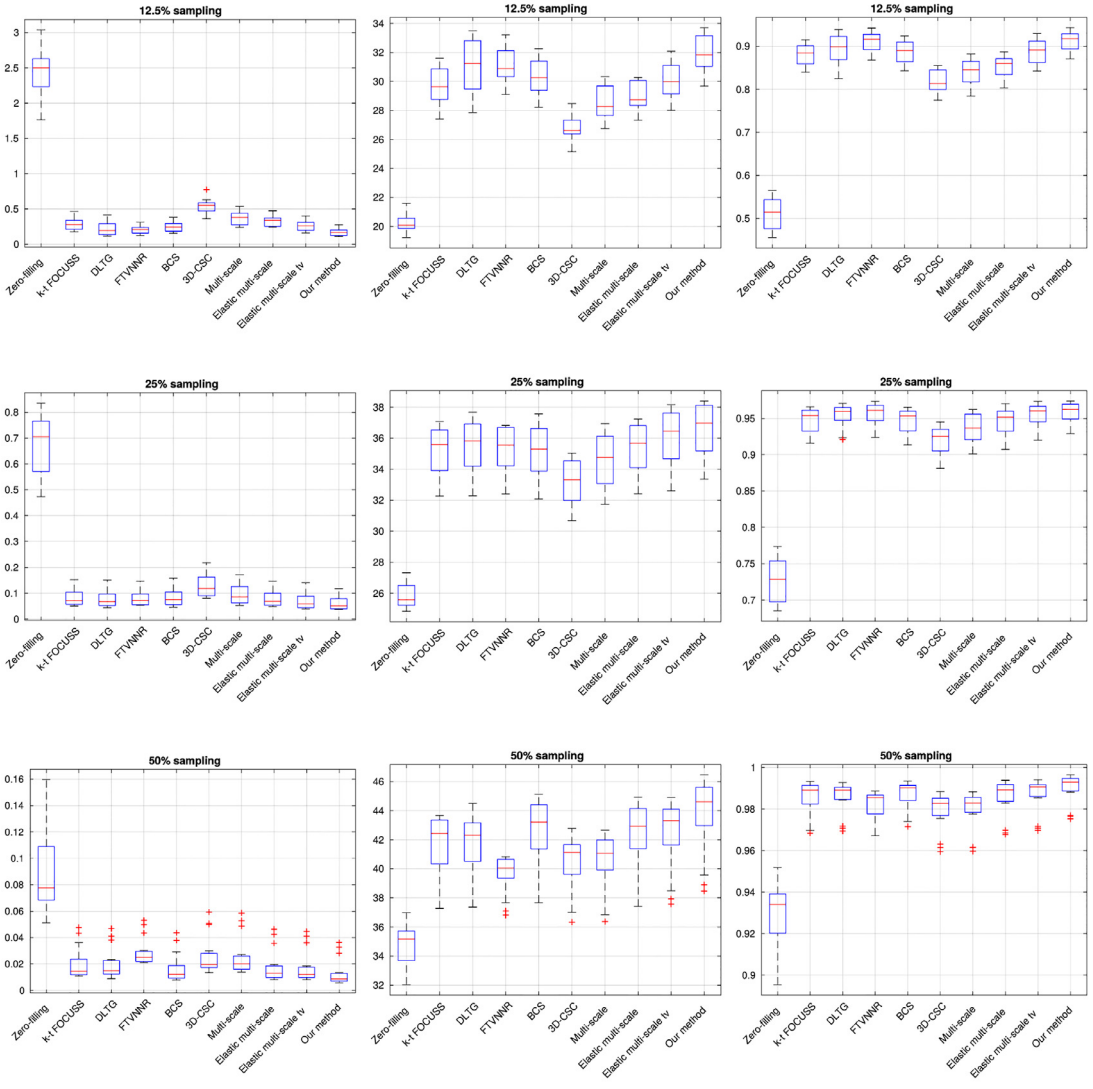

(a) MSEs (b) PSNRs; unit:dB (c) SSIMs

Fig. 5. MSEs, PSNRs, and SSIMs evaluation in three different sampling rates on cardiac MRIs (first column: MSEs; second column: PSNRs; third column: SSIMs).

where m^h is equal to $m - R\mathcal{F}_2 s^l$. The g and d variables are related by a projection operator as a combination of a truncated matrix with the corresponding dictionary size followed by a padding-zero in order to make the dimension of g the same as that of x, and the variable g should also be zero-padded to make its size similar to g_{f_3} and x_{f_3} so we can leverage Fourier transform to solve this problem. The constrained Eq. (10) can be unconstrained by using dual variable u, h, and further regulates the measurement consistency and the dual differences with γ, ρ and σ, respectively:

$$\begin{aligned}\min_{d,x,g,y,s^h} \frac{\alpha}{2}\left\| s^h - \sum\sum d * x \right\|_2^2 + \lambda_1\|y\|_1 + \frac{\lambda_2}{2}\|y\|_2^2 \\ + \frac{\gamma}{2}\|R\mathcal{F}_2 s^h - m^h\|_2^2 + \frac{\rho}{2}\|x - y + u\|_2^2 \\ + \frac{\sigma}{2}\|d - g + h\|_2^2 \; s.t. : g = Proj(d), \|g\|_2^2 \le 1 \end{aligned} \tag{11}$$

We solve Eq. (11) by iteratively finding the minimization solution of subproblems, as shown below:

Solve for x:

$$\min_x \frac{\alpha}{2}\left\| \sum\sum d * x - s^h \right\|_2^2 + \frac{\rho}{2}\|x - y + u\|_2^2 \tag{12}$$

We apply the Fourier transform to subproblem (12), it becomes:

$$\min_{x_{f_3}} \frac{\alpha}{2}\left\| \sum\sum d_{f_3} x_{f_3} - s^h_{f_3} \right\|_2^2 + \frac{\rho}{2}\|x_{f_3} - y_{f_3} + u_{f_3}\|_2^2 \tag{13}$$

Next, the minimum solution can be found by taking the derivative of Eq. (13) with respect to variable x_{f_3} and setting it to zero. The solution is shown in Eq. (14).

$$(\alpha D^H_{f_3} D_{f_3} + \rho I) x_{f_3} = D^H_{f_3} s^h_{f_3} + \rho(y_{f_3} - u_{f_3}) \tag{14}$$

where D_{f_3} is the concatenation of all diagonalized matrices $d_{f_3\ n,k}$, as illustrated in Eq. (15) and $D^H_{f_3}$ is the Hermitian transpose of D_{f_3}.

$$D_{f_3} = [diag(d_{f_3\ 1,1}), \ldots, diag(d_{f_3\ 1,k}), \ldots, diag(d_{f_3\ n,k})] \tag{15}$$

Solve for y:

$$\min_y \lambda_1\|y\|_1 + \frac{\lambda_2}{2}\|y\|_2^2 + \frac{\rho}{2}\|x - y + u\|_2^2 \tag{16}$$

In Bristow et al. (2013); Wohlberg (2014); Quan and Jeong (2016a,b), l_1 regularization is only used for CSC; however, our subproblem contains both lasso and ridge regularizations. Fortunately,

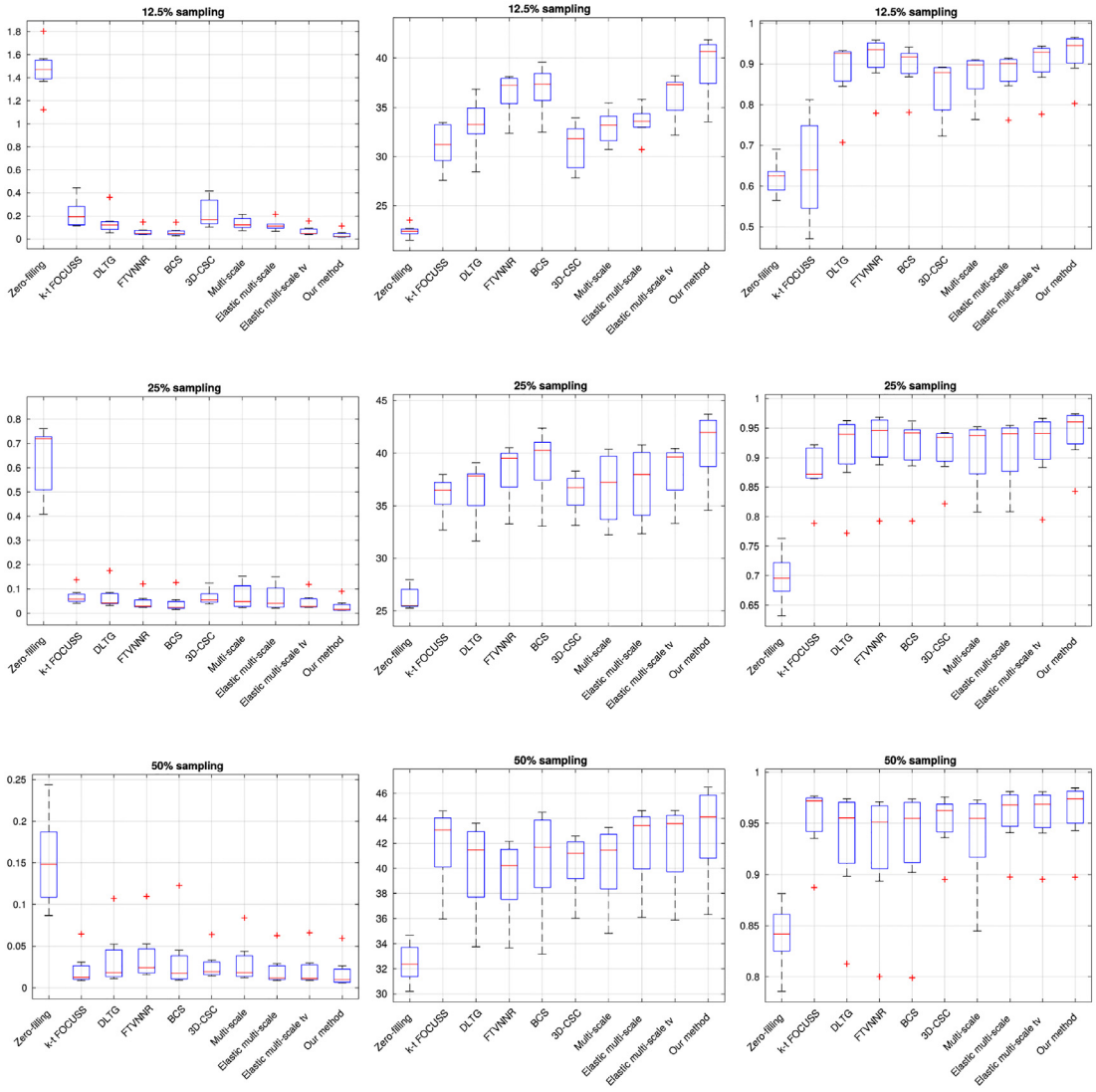

(a) MSEs (b) PSNRs; unit:dB (c) SSIMs

Fig. 6. MSEs, PSNRs, and SSIMs evaluation in three different sampling rates on tumor DCE MRIs (first column: MSEs; second column: PSNRs; third column: SSIMs).

this subproblem can also be solved by using a shrinkage operation:

$$y = S_{\lambda_1/(\lambda_2+\rho)}\left(\frac{\rho(x+u)}{\lambda_2+\rho}\right) \tag{17}$$

Update for u:

The update rule for u can be defined as a fixed-point iteration with the difference between x and y (u converges when x and y converge each other).

$$u = u + x - y \tag{18}$$

Solve for d:

$$\min_d \frac{\alpha}{2}\left\| \sum\sum d * x - s^h \right\|_2^2 + \frac{\sigma}{2}\|d - g + h\|_2^2 \tag{19}$$

We solve this subproblem in the Fourier domain, similar to x:

$$\min_{d_{f_3}} \frac{\alpha}{2}\left\| \sum\sum d_{f_3} x_{f_3} - s^h_{f_3} \right\|_2^2 + \frac{\sigma}{2}\|d_{f_3} - g_{f_3} + h_{f_3}\|_2^2 \tag{20}$$

$$\left(\alpha X^H_{f_3} X_{f_3} + \sigma I\right) d_{f_3} = X^H_{f_3} s^h_{f_3} + \sigma\left(g_{f_3} - h_{f_3}\right) \tag{21}$$

Note that X_{f_3} stands for the concatenated matrix of all diagonal matrices $x_{f_3\ n,k}$ as shown in Eq. (22) and $X^H_{f_3}$ is the Hermitian transpose of X_{f_3}.

$$X_{f_3} = [diag(x_{f_3\ 1,1}), \ldots, diag(x_{f_3\ 1,k}), \ldots, diag(x_{f_3\ n,k})] \tag{22}$$

Solve for g:

$$\min_g \frac{\sigma}{2}\|d - g + h\|_2^2 \ s.t.: \ g = Proj(d), \|g\|_2^2 \le 1 \tag{23}$$

g can be solved by using the inverse Fourier transform of d_{f_3}. This projection should be constrained by suppressing the elements which are outside the filter size $d_{n,k}$, and followed by normalizing its l_2-norm to a unit length.

Update for h: Similar to u, we update h as follows:

$$h = h + d - g \tag{24}$$

Solve for s^h:

$$\min_{s^h} \frac{\alpha}{2}\left\| s^h - \sum\sum d * x \right\|_2^2 + \frac{\gamma}{2}\|R\mathcal{F}_2 s^h - m^h\|_2^2 \tag{25}$$

Subproblem (25) can be transformed and solved in the 2D Fourier domain:

$$\min_{s^h_{f_2}} \frac{\alpha}{2}\left\| s^h_{f_2} - \mathcal{F}_2^H \sum\sum d_{f_3} x_{f_3} \right\|_2^2 + \frac{\gamma}{2}\|R s^h_{f_2} - m^h\|_2^2 \tag{26}$$

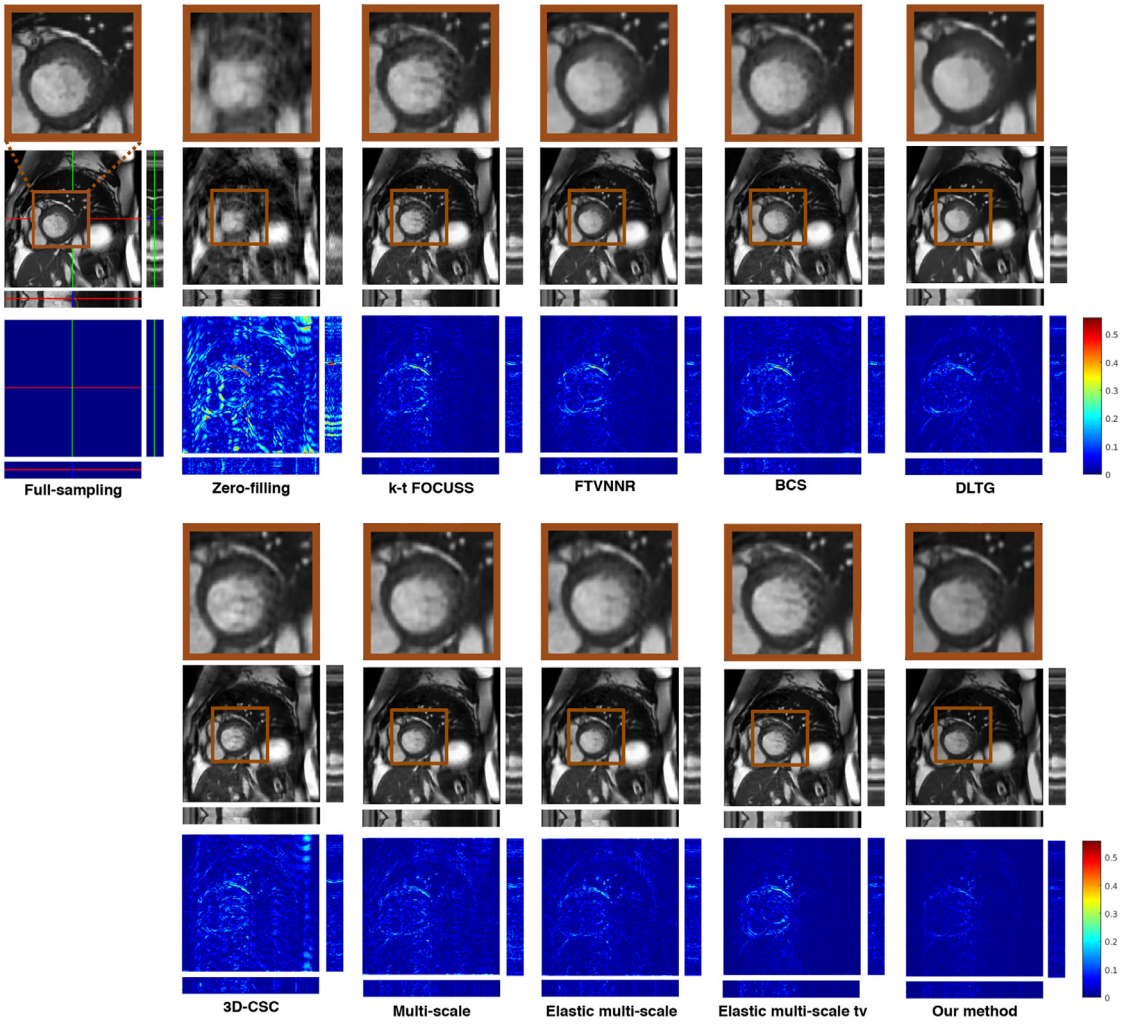

Fig. 7. Image quality and pixel-wise error comparison of various reconstruction methods on Cardiac 2 dataset (12.5% sampling).

Previously, d_{f_3} and x_{f_3} were obtained in the 3D Fourier domain, we must bring it onto the same space by applying an inverse Fourier transform along the time-axis $\mathcal{F}_2^H$. Finally, $s^h_{f_2}$ can be found by solving the following linear system:

$$(\gamma R^H R + \alpha I) s^h_{f_2} = \gamma R^H m^h + \alpha \mathcal{F}_2^H \sum \sum d_{f_3} x_{f_3} \qquad (27)$$

Note that we can efficiently solve independent linear systems (14), (21), and (27) via the Sherman-Morrison formula, as shown in Wohlberg (2014). After the iteration process, s^h will be the results of applying a 2D inverse Fourier transform $\mathcal{F}_2^H$ to $s^h_{f_2}$.

3.1.3. Complexity analysis of the reconstruction algorithm

The proposed iterative reconstruction method consists of a spectral decomposition using a low-pass filter and solving sub-optimization problems. In order to investigate the time complexity of the proposed method, we carefully analyze these components using Big $\mathcal{O}$ Notation, as shown in Table 1. Suppose that P is the number of pixels in a dynamic MR image and M is the total number of convolutional filters ($M = N \times K$ where N is the number of levels and K is the number of filters in each level.). Firstly, the cost of a fast Fourier transform (FFT) of the MR image is $\mathcal{O}(PlogP)$. In the spectral decomposition step, low-pass filtering is used to separate high- and low-frequency components of MR data in a frequency domain, which requires forward and inverse Fourier transforms ($\mathcal{O}(PlogP)$). Temporal TV minimization (s^l) step contains FFTs, a total variation operator and a clipping operator, which cost $\mathcal{O}(PlogP)$, $\mathcal{O}(P)$ and $\mathcal{O}(P)$, respectively. Solving subproblems x, d and s^h Eqs. (14), (21) and (27) can be efficiently solved using the Sherman-Morrison formula in $\mathcal{O}(MP)$ time (Wohlberg, 2016). However, each subproblem requires per-dictionary forward and inverse Fourier transforms to apply the convolution operators in frequency domain, which becomes the dominant cost ($\mathcal{O}(MPlogP)$). Similarly, solving the subproblem g requires per-dictionary FFTs, which costs $\mathcal{O}(MPlogP)$. Finding solution for y requires applying the shrinkage operation to every element in y; thus, it costs $\mathcal{O}(MP)$. Finally, the addition and subtraction operations for updating u and h cost $\mathcal{O}(MP)$. In conclusion, the asymptotic time complexity of the proposed method is the upper bound of the time complexity of subproblems, which is $\mathcal{O}(MPlogP)$.

Table 1
Time complexity analysis of the proposed method.

Component	Complexity
Spectral decomposition Eq. (1)	$\mathcal{O}(PlogP)$
Solve s^l Eq. (7)	$\mathcal{O}(PlogP)$
Solve x, d and s^h Eqs. (14), (21) and (27)	$\mathcal{O}(MPlogP)$
Solve g	$\mathcal{O}(MPlogP)$
Solve y Eq. (17)	$\mathcal{O}(MP)$
Update u and h Eqs. (18) and (24)	$\mathcal{O}(MP)$

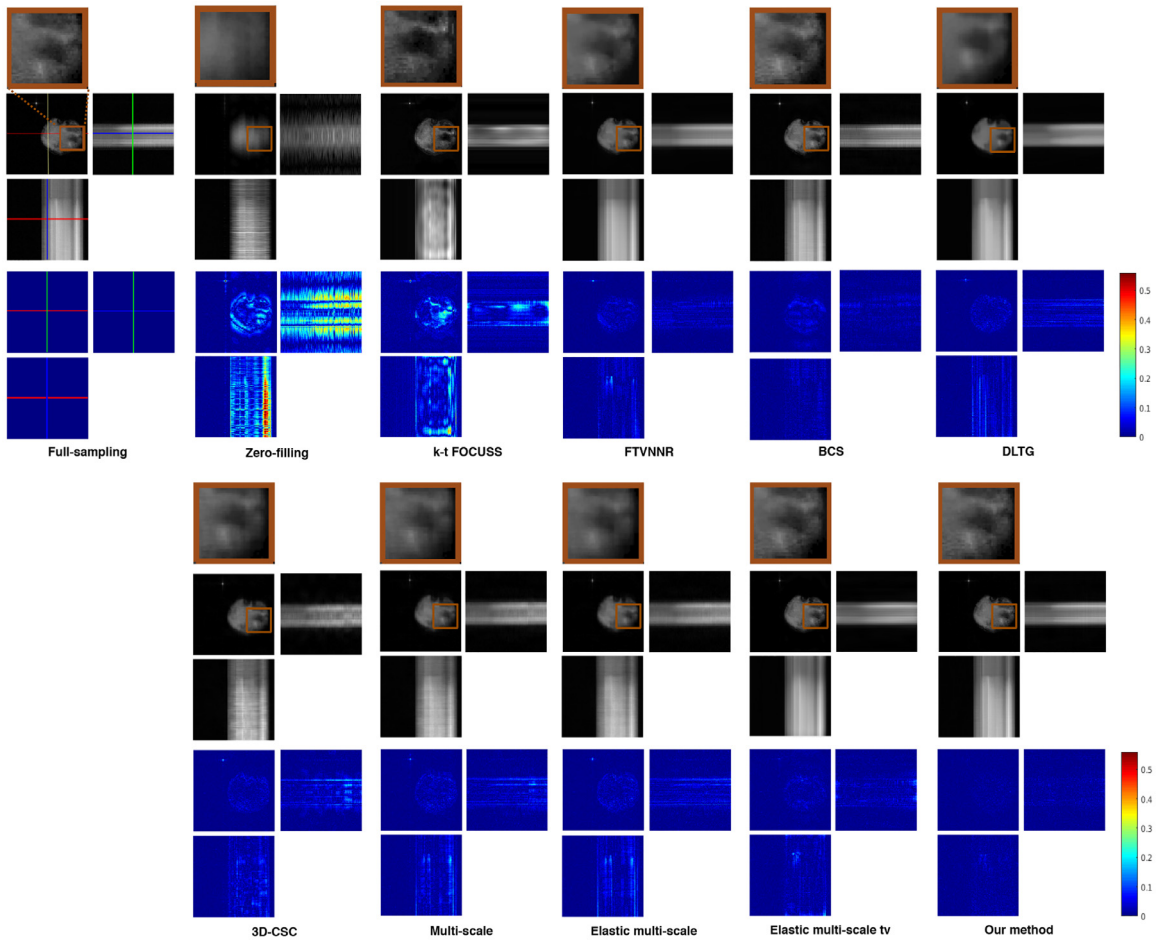

Fig. 8. Image quality and pixel-wise error comparison of various reconstruction methods on Tumor 2 dataset (12.5% sampling).

3.2. Parameter searching process

The proposed reconstruction process contains many user-controllable parameters (e.g., α, γ, λ_1, λ_2, ρ, σ, θ, D_0 and n), and manually adjusting these parameters is a time-consuming and laborious process. Thus, we propose an automatic parameter searching process, which can be thought of as a pre-processing step of the reconstruction process. Our searching approach employ a GA, which is a meta-heuristic algorithm inspired by the process of natural evolution, as shown in Fig. 3. In the proposed parameter searching process, we create a simulation based on the objective function which is defined by a fully-sampled k-space data and an undersampling mask, and a GA finds the best parameters to minimize this objective function.

A detailed description of the parameter selection process is introduced below. First, the full (ground-truth) image is under-sampled to generate zero-filling reconstruction using the same sampling mask used in the reconstruction process. Then, GA arbitrarily initializes a population with L members where each individual (i) has a set of nine randomly chosen parameters to be used in the reconstruction process. Next, the zero-filling is reconstructed L times by using our method (Fig. 1 yellow box) that each time uses a set of nine parameters which contents in every individual (i) of the current population to get reconstructed results (z). The fitness values of objective function f are then calculated for each member in the current population by comparing between the full-sampled and reconstructed image (z) as well as sparse code x. After ward, GA selects members, called parents, based on the ranking of their calculated fitness values. Finally, there are three types of children that are generated for the next generation such as elite children with the best fitness values, crossover children created by combining a pair of parents and mutation children created by introducing random changes to a single parent. The algorithm continues by creating a loop of generating the new generation based on bio-operators until reaching the terminate condition (i.e., the current generation is greater than pre-defined number). In general, the goal of GA in optimization problem is conducting many trials and errors to find the best individual which minimizes the fitness function. Therefore, we propose a fitness function (f), as shown in Eq. (28), that uses Peak Signal-To-Noise-Ratio ($PSNR$) between the CS-reconstruction result, the full reconstruction, and the average value of sparse codes ($\bar{x}$) which are outputs of the reconstruction process (Fig. 1 yellow box) after 100 iterations.

Table 2
Lower and upper bounds of parameters used in our experiment.

	α	γ	λ_1	λ_2	ρ	σ	θ	D_0	n
Lower	0.001	0.001	0.001	0.001	1	1	0.001	1	1
Upper	5	5	5	5	100	100	1	5	5

$$f = -PSNR + \tau\bar{x} \tag{28}$$

where τ is the weight for trade-off between 2 values $PSNR$ (bigger is better) and average of x (smaller is better). Moreover, we also set possible lower and upper bounds for each parameter to narrow down the GA's searching space, as illustrated in Table 2. Specially, our experiment shows that a GA can be applied only once to find

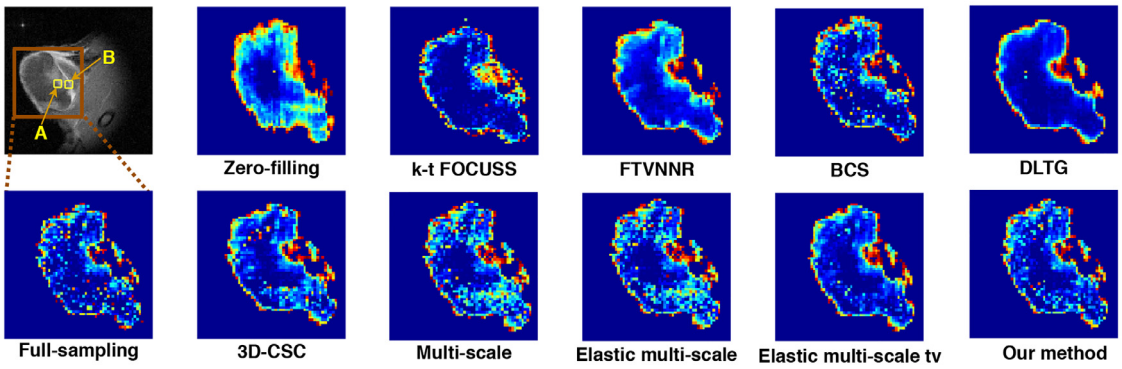

(a) Ak_{ep} maps of 25% sampling reconstruction of Tumor 1 dataset

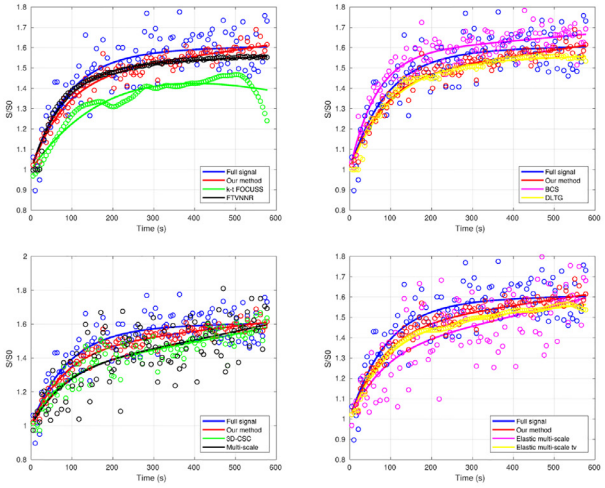

(b) Temporal profile of A

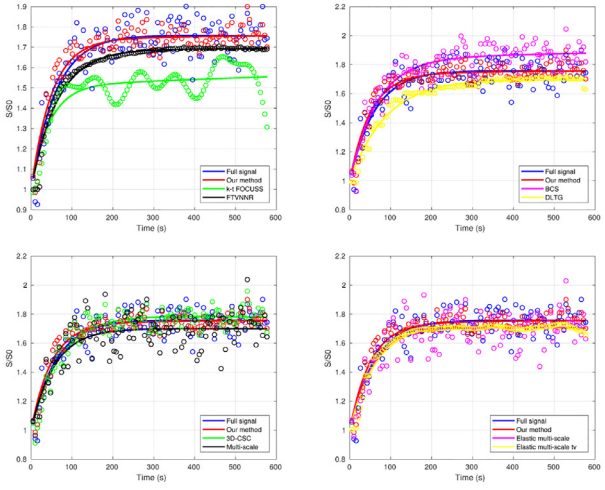

(c) Temporal profile of B

Fig. 9. Reconstruction quality comparison of Tumor 1 dataset.

the optimal parameters that work for similar types of data (i.e., cardiac or DCE MRI data).

4. Experiment results

To assess the performance of our method, we conducted experiments on 15 cardiac MRI datasets from The Data Science Bowl (Kaggle, 2015) (30 frames of a 256×256 image across the cardiac cycle of a heart for each dataset), 7 tumor DCE MRI datasets (128×128 image with 128 frames of each dataset) and a multi-coil MRI brain dataset (CBIG, 2018) (128×128 with 12 frames in which each frame consists of 12 parallel acquisitions) in three different rates of Cartesian k-space undersampling masks (12.5%, 25% and 50% sampling masks), as shown in Fig. 4c. GA is also set to run only one time to search parameters in five generations with $L = 200$ and $\tau = 20$. More specifically, for each

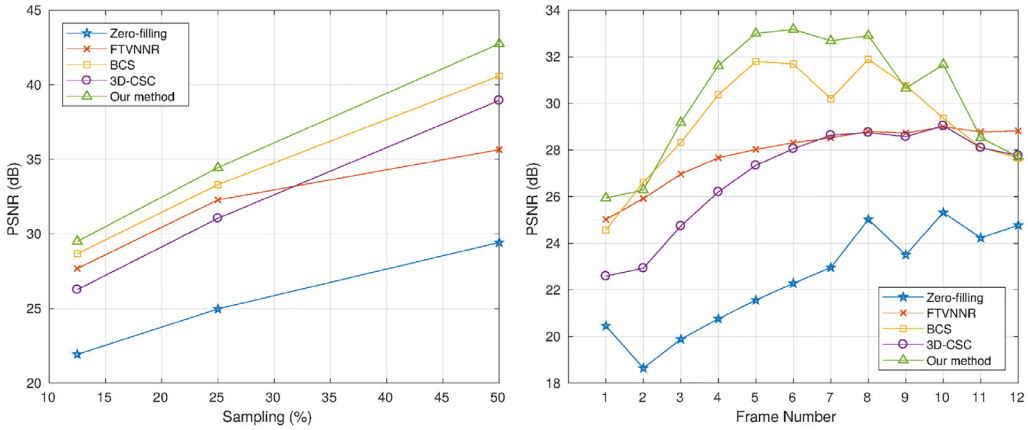

(a) Average PSNRs of all frames (b) PSNRs of frames at 12.5% mask

Fig. 10. PSNRs evaluation on the multi-coil MRI brain dataset.

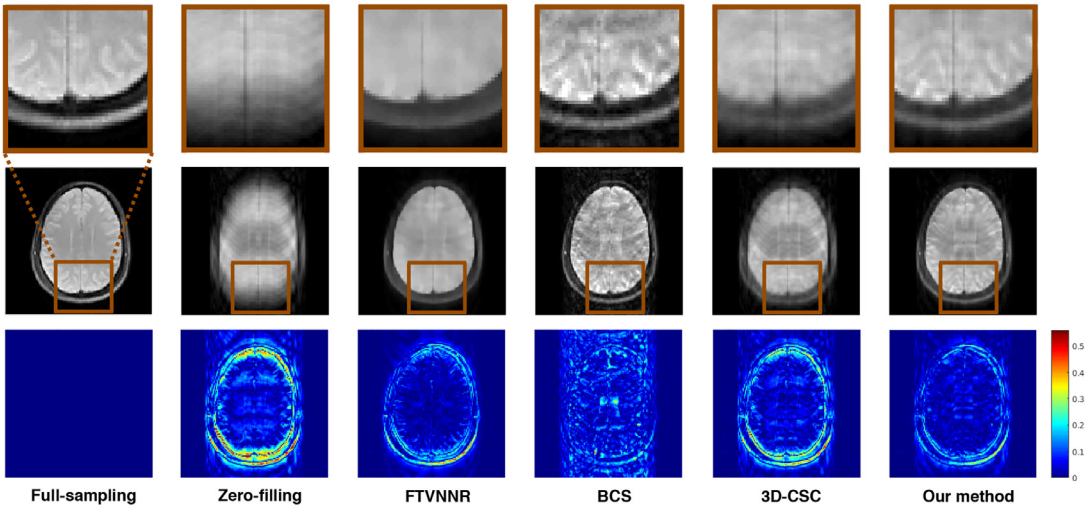

Fig. 11. Image quality and pixel-wise error comparison of multi-coil reconstruction methods on the brain dataset (12.5% sampling).

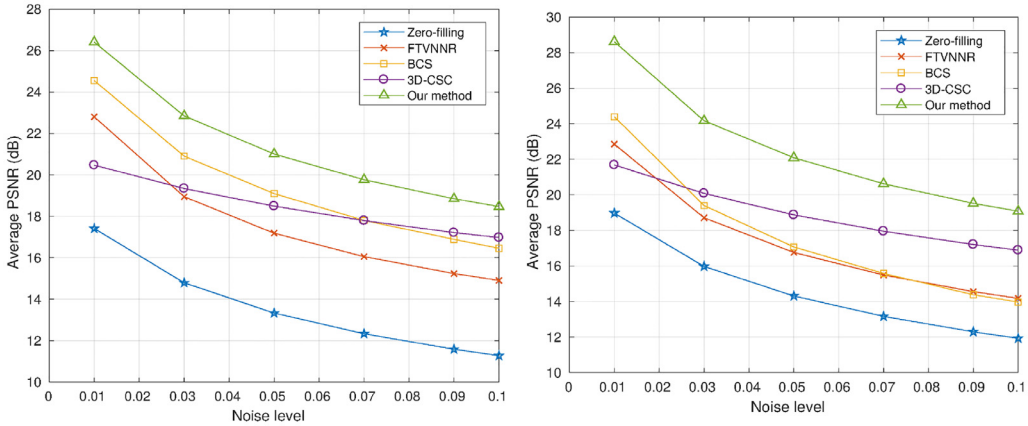

(a) Cardiac MRI (b) DCE tumor MRI

Fig. 12. Average PSNRs of the images reconstructed from the various noise-corrupted k-space data.

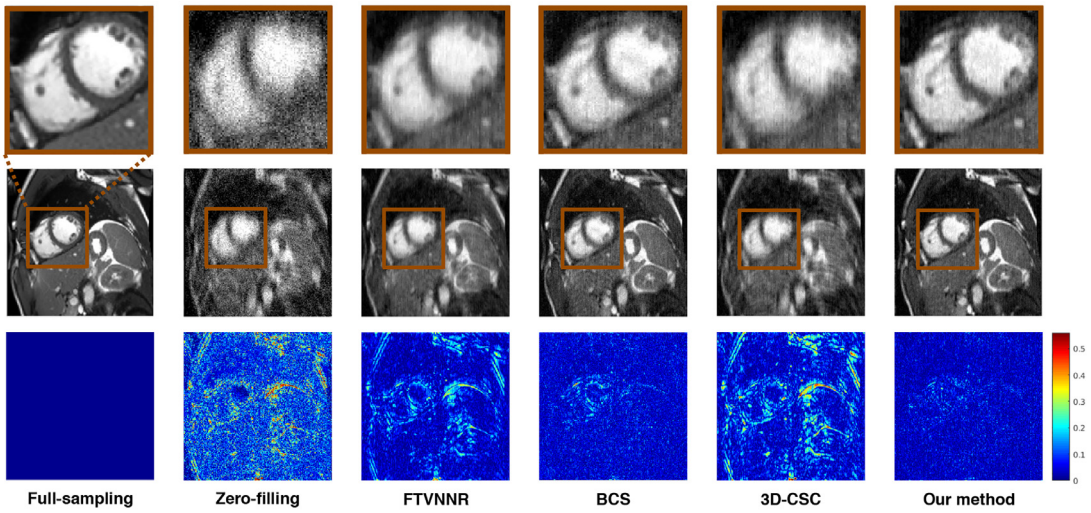

Fig. 13. Reconstruction of noise-corrupted Cardiac 3 dataset (at noise level 0.01).

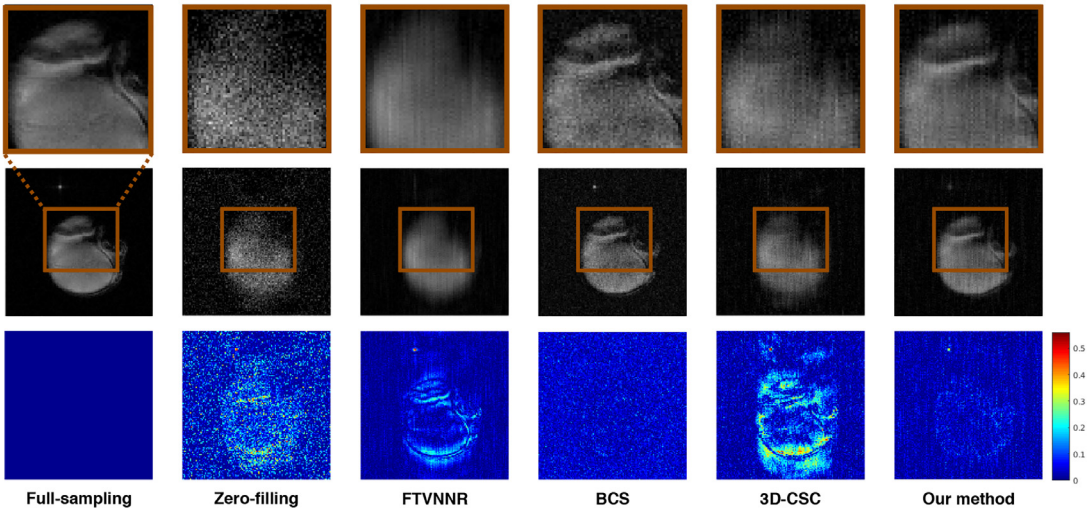

Fig. 14. Reconstruction of noise-corrupted DCE tumor 3 dataset (at noise level 0.01).

kind of dataset, we arbitrarily select one full-sampled data and the sampling mask to optimize parameters, and reuse these found parameters to reconstruct the remaining of MRI datasets. We compare our method with several state-of-the-art methods, including $k-t$ FOCUSS (Jung et al., 2009), FTVNNR (Yao et al., 2018), BCS (Lingala and Jacob, 2013), Caballero et al. (Caballero et al., 2014), and 3D CSC (Quan and Jeong, 2016a). We also compare with the intermediate versions of our method (i.e., incrementally adding new features, such as multi-scale extension of CSC, elastic net regularization, and spectral decomposition, to the baseline version of 3D CSC (Quan and Jeong, 2016a) to assess how each addition of feature affects the overall performance of the method (see Table 3). The proposed prototype system is implemented using MATLAB 2017a with GPU support.

4.1. Reconstruction quality evaluation

For a fair comparison, we set up all DLTG (Caballero et al., 2014) and CSC methods with the same number of filters (27 filters). All multi-scale 3D CSC methods used three different filter sizes ($N = 3$) and each size contained nine convolutional filters ($K = 9$). The box-plots below illustrate achievements of Mean Square Errors (*MSEs*), Peak Signal-To-Noise-Ratios (*PSNRs*) and Structural SIMilarities (*SSIMs*) for cardiac and tumor DCE MRIs; on each box, the central mark indicates the median, and the bottom and top edges of the box indicate the 25th and 75th percentiles, respectively. As can be seen in Figs. 5 and 6, our method gives a higher *PSNR, SSIM* and a lower *MSE* compared to the other approaches in case of 12.5%, 25%, 50% sampling rates. Figs. 7 and 8 show a qualitative comparison of various reconstruction results. It is shown that our method generates less visual artifact compared to other methods (see the region of interests and pixel-wise error maps), even under an extremely low sampling rate (12.5%). It is also worth noting that our method can reconstruct temporal changes in DCE data more accurately compared to $k-t$ FOCUSS and DLTG at a very low sampling rate (see Fig. 6 12.5%).

The Ak_{ep} value, borrowed from the Hoffmann et al. (1995)'s model, is also a commonly used quality metric for dynamic MRI (especially DCE) to judge the consistency of the reconstructed image sequence because this value reflects the degree of MRI signal enhancement and the exchange rate in term of brightness and the contrast. Therefore, Ak_{ep} value characterizes the velocity of MRI signal change in the region of interest (ROI) of the tumor, which is shown to provide the relevant information regarding tumor perfusion and permeability. To assess how the proposed reconstruction method performs, we measure the Ak_{ep} on each reconstructed

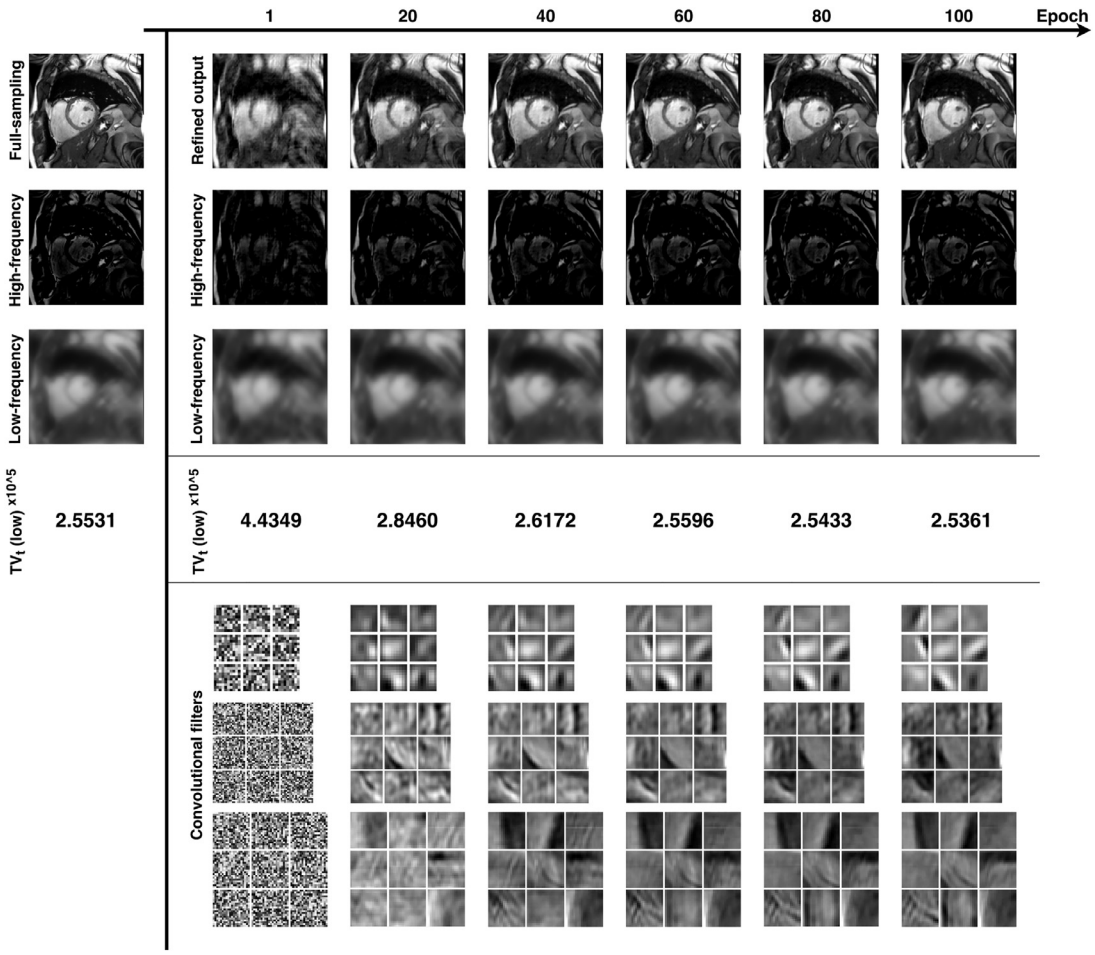

Fig. 15. Convergence of proposed method for reconstructing 12.5% sampling Cardiac 1 dataset over 100 epochs.

Table 3
CS-MRI reconstruction methods compared in our experiment.

Method	Abbreviation
$k-t$ FOCUSS (Jung et al., 2009)	$k-t$ FOCUSS
Algorithm using low-rank and total variation regularizations (Yao et al., 2018)	FTVNNR
Blind compressive sensing (Lingala and Jacob, 2013)	BCS
Caballero et al. (2014)	DLTG
3D CSC (Quan and Jeong, 2016a)	3D-CSC
Multi-scale 3D CSC	Multi-scale
Multi-scale 3D CSC with l_1, l_2 regularization	Elastic multi-scale
Elastic multi-scale and temporal TV minimization	Elastic multi-scale tv
Elastic multi-scale on high-frequency, and temporal TV minimization on low-frequency	Our method

image (actually, Ak_{ep} is generated per pixel) and generate a least-square fitting curve. By comparing the curve's shape, we can verify the reconstruction methods efficacy. The Fig. 9a shows Ak_{ep} values as a color map of Tumor 1 dataset in Fig. 4b where our result clearly preserves details much better than the others and Fig. 9b and c shows the curve fitting profiles at some locations (marked A and B in Fig. 9a). As illustrated, our curve fitting profiles closely approximate the ground truth (full signal). In addition, our method effectively reduces the intensity variation (or noise) of the reconstructed images (see the variation of red circles are much smaller than that of other results) due to enforcing temporal coherence using a TV energy.

Overall, the proposed method achieves better reconstruction quality than other state-of-the-art methods. Shift-invariant convolution filters can represent both spatial and temporal features well, whilst multi-scale 3D CSC with l_1 and l_2 regularization shows its performance with better *MSE, PSNR* and *SSIM*. Moreover, our frequency-splitting reconstruction approach, using temporal TV minimization for low-frequency and multi-scale 3D CSC with elastic net regularization for high-frequency, can significantly improve the image quality as well as convergence rate, which will be discussed in Section 4.4.

4.2. Extension to multi-coil parallel MR

Although we introduced our method for single coil MRI data in the previous sections, the proposed method can be applied to multi-coil MRI data as well with a small modification. For this, the main objective function Eq. (4) can be combined with SENSE in the $k-t$ SPARSE-SENSE framework (Otazo et al., 2010) by multiplying the coil sensitivity matrix E after the undersampled Fourier trans-

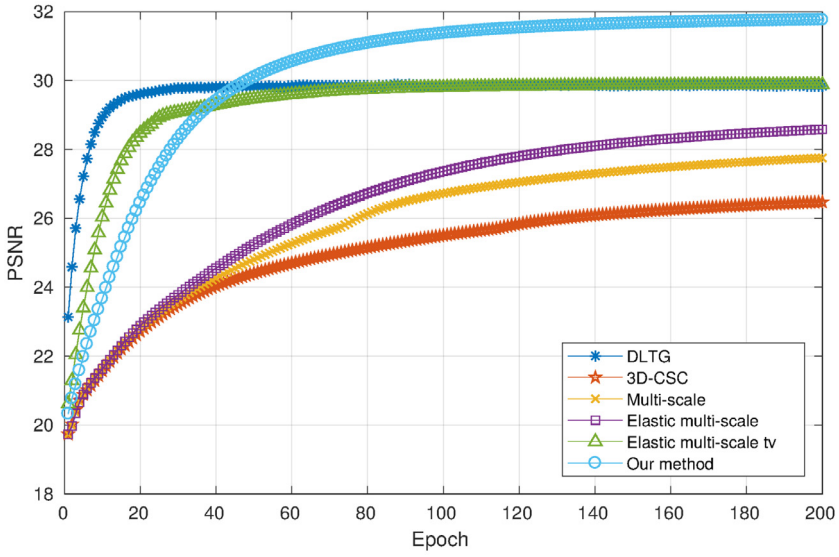

(a) Cardiac 2 dataset

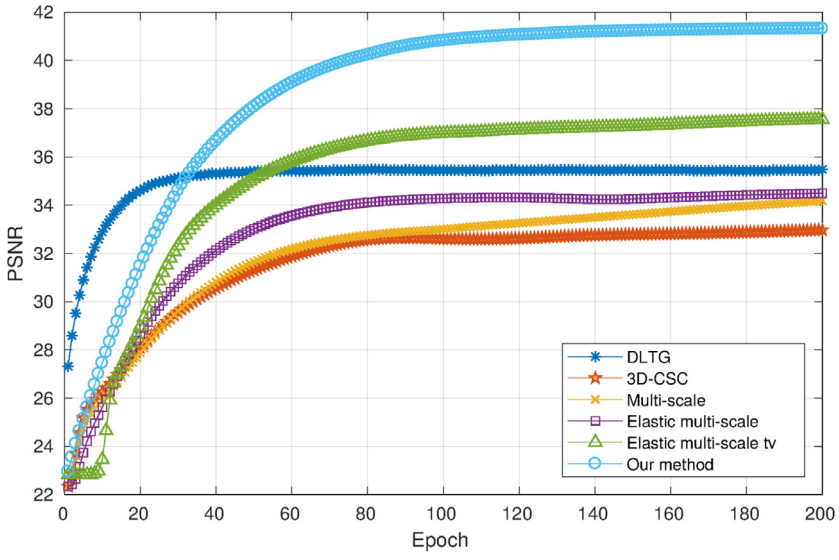

(b) Tumor 2 dataset

Fig. 16. Convergence rate comparison of 12.5% sampling Cardiac 2 and Tumor 2 datasets in terms of PSNRs.

form as shown in Eq. (29) below:

$$\min_{d,x,s_e^h,s_e^l} \frac{\alpha}{2}\left\|s_e^h - \sum_n^N \sum_k^K d_{n,k} * x_{n,k}\right\|_2^2 + \lambda_1 \sum_n^N \sum_k^K \left\|x_{n,k}\right\|_1 + \frac{\lambda_2}{2} \sum_n^N \sum_k^K \left\|x_{n,k}\right\|_2^2 + \theta \left\|\nabla_t s_e^l\right\|_1$$
$$s.t.: \|R\mathcal{F}_2(s_e^h + s_e^l) - m\|_2^2 < \epsilon^2, \|d_{n,k}\|_2^2 \le 1 \quad (29)$$

where $s_e^h = Es^h$ and $s_e^l = Es^l$.

We tested the parallel version of our method on a 12-coil MRI brain dataset, and compared with FTVNNR, BCS and 3D-CSC methods for image quality assessment. For all sampling rates we tested (12.5%, 25% and 50%), our method outperformed the other methods (i.e., higher PSNR of reconstructed images, see Fig. 10a and b). Fig. 11 also shows that our method is less prone to pixel-wise errors and generates images closer to the full reconstruction than FTVNNR, BCS and 3D-CSC.

4.3. Robustness to noise

Noise resiliency is another important quality measure for the MR image reconstruction algorithm. To assess the noise resiliency of the proposed method, we synthetically corrupted the undersampled k-space data with Gaussian random noise and compared the reconstruction quality. In this experiment, we used cardiac and DCE MRI datasets at three Cartesian sampling rates, corrupted with Gaussian white noise in various levels (the range of standard deviation of Gaussian is {0.01, 0.03, 0.05, 0.07, 0.09, 0.1}), as shown in Fig. 4c. We compared the reconstruction results with those of three representative methods (FTVNNR (Yao et al., 2018), BCS (Lingala and Jacob, 2013) and 3D-CSC (Quan and Jeong, 2016a)) because they represent general transformation (non-learning approach), patch-based dictionary learning, and convolutional sparse coding, respectively. The optimal parameters found in the previous experiments (Section 4.1) are used for all methods in this ex-

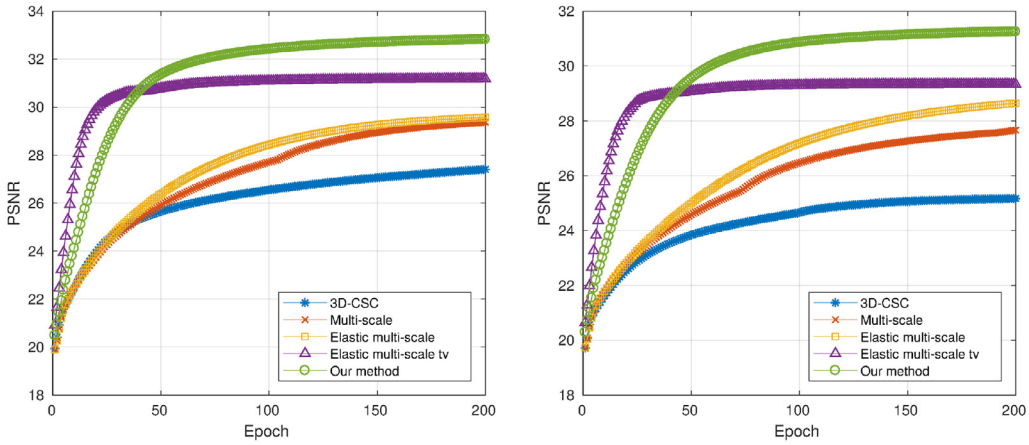

(a) Convergence curves of two different Cardiac 3 and 4 datasets

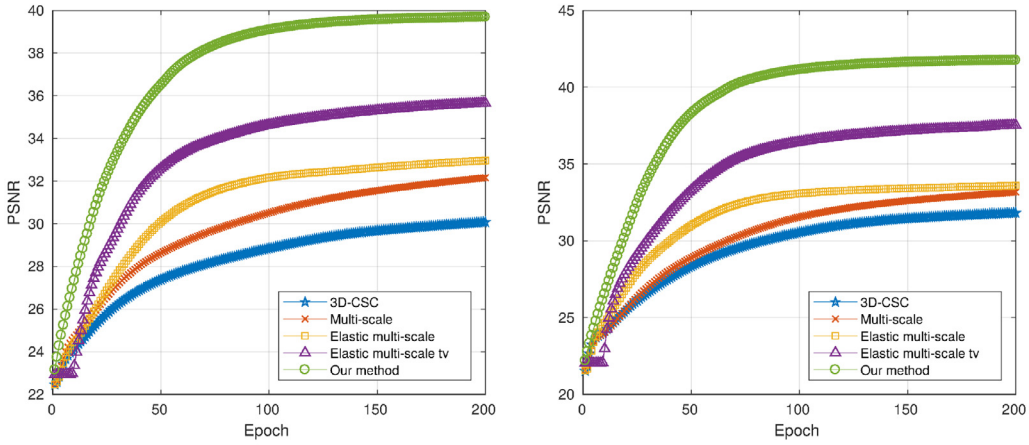

(b) Convergence curves of two different Tumor 3 and 4 datasets

Fig. 17. Convergence curves of 12.5% sampling cardiac and tumor data in terms of PSNRs using the optimal parameters found by the genetic algorithm.

periment. As shown in Figs. 12, 13 and 14, our method produced the results with much higher PSNR, less noise, and superior image quality compared to the other methods.

4.4. Convergence evaluation

Fig. 15 illustrates the convergence of our method over 100 iterations. The left column contains full low-frequency, full high-frequency, full reconstruction and total time-axis gradient value of full low frequency, whilst right column gives the changing of refined output with its low- and high-frequency as well as the convolutional filters and temporal total variation value. In Fig. 15, the features in high-frequency part are progressively refined along with converging of convolutional filters every twenty epochs. The temporal total variation value in low-frequency also reduces over iterations which enforces the coherence of time-axis. As seen in Figs. 16 and 17, using temporal TV minimization is clearly helpful for the reconstruction process, while our frequency splitting approach can significantly improve the quality with comparable convergence rate. The proposed method converges faster (i.e. require less number of epochs) than 3D-CSC, multi-scale and elastic multi-scale. Note that patch-based dictionary (DLTG (Caballero et al., 2014)) usually converges faster, but the actual running time is much slower because there is no GPU acceleration as in our method (see Table 4). Moreover, Figs. 16 and 17 show adequate convergence curves of the CSC methods with a large *PSNR* improvement and no divergence. Thus, GA can find optimal parameters for the reconstruction process. In our observation, when we used the searched parameters for all datasets in the same kind of MRIs, the efficiency of convergence rate still remains, as shown in Fig. 17.

4.5. Running time evaluation

We measured the average reconstruction time of methods on a PC equipped with an Intel i7-7700K CPU and a NVIDIA Titan X GPU. All CSC approaches and DLTG (Caballero et al., 2014) were run for 200 epochs, as shown in Figs. 16 and 17; however, the rate of convergence varied over methods. For example, our method converged in about 130 epochs, while DLTG took about 40 epochs (see Fig. 16) and 3D-CSC took more than 185 epochs (see Fig. 17). As shown in Table 4, the average per-epoch running time of our method on a GPU is 36.9 ×, 84 ×, 5 ×, and 16.5 × faster than BCS, DLTG, 3D-CSC (CPU) and the CPU version of our method, respectively. A similar performance gain of our method was observed on DCE MRI data and multi-coil brain MRI date as well. Furthermore, DLTG converged faster (i.e., small number of epochs) than our method, but the actual running time of our method on a GPU to reach the convergence was significantly faster than that of DLTG (speed up of 25.58 × for cardiac and 23 × for DCE data). However, due to the computational overhead of our method (e.g., frequency filtering and energy optimization in low- and high-frequency),

Table 4
Average running time of various reconstruction methods (per epoch: average running time of one epoch; total time: average running time to reach the convergence).

	Cardiac dataset (second)		DCE dataset (second)		Brain dataset (second)	
	Per epoch	Total time	Per epoch	Total time	Per epoch	Total time
$k-t$ FOCUSS (CPU)	_	177.6	_	256.2	_	_
FTVNNR (CPU)	_	131.1	_	151.5	_	65.1
BCS (CPU)	41.05	410.5	54.01	540.1	29.1	290.1
DLTG (CPU)	66.12	2644.8	76.97	3078.8	_	_
3D-CSC (CPU)	3.94	728.9	5.86	1084.1	2.875	474.38
Our method (CPU)	12.96	1684	18.35	2385.5	6.87	1099.2
3D-CSC (GPU)	0.503	93.06	0.728	134.68	0.361	57.76
Our method (GPU)	0.787	102.31	1.029	133.77	0.403	64.5

single-scale 3D CSC on a GPU was faster than our method. We also expect a significant performance improvement using NVIDIA CUDA and C/C++ over the current implementation using MATLAB, which is left for the future work.

5. Conclusion

In this paper, we introduced a novel CS-MRI reconstruction workflow based on an unsupervised learning approach. We discovered that the frequency-dependent reconstruction, i.e., using temporal total variation for low-frequency reconstruction and multi-scale 3D CSC with elastic net regularization for high-frequency reconstruction, played an important role for improving the overall reconstruction quality and the convergence rate. The proposed automatic parameter searching method using GA significantly reduced user's effort for tuning parameters in the reconstruction process. Furthermore, we showed that the proposed method can be easily extended to parallel MR imaging. The results showed that the proposed method outperformed the state-of-the-art CS-MRI reconstruction methods, such as $k-t$ FOCUSS (Jung et al., 2007, 2009), FTVNNR (Yao et al., 2018), single-scale 3D CSC (Quan and Jeong, 2016a), blind compressive sensing (Lingala and Jacob, 2013) and patch-based dictionary learning (Caballero et al., 2012, 2014), in terms of image quality and noise resiliency. In the future, we plan to improve the speed of proposed method by leveraging the parallel computing technology, such as multi-GPU and cluster systems. Exploring advanced meta-heuristic algorithms to improve the parameter selection process is another interesting future research direction.

Acknowledgments

This research was partially supported by the Bio & Medical Technology Development Program of the National Research Foundation of Korea (NRF) funded by the Korean government, MSIT (NRF-2015M3A9A7029725), the Next-Generation Information Computing Development Program through the NRF funded by the MSIT (NRF-2016M3C4A7952635), and the Basic Science Research Program through the NRF funded by the Ministry of Education (NRF-2017R1D1A1A09000841).

References

Aharon, M., Elad, M., Bruckstein, A., 2006. K-SVD: An algorithm for designing overcomplete dictionaries for sparse representation. IEEE Trans. Signal Process. 54 (11), 4311–4322.
Awate, S.P., DiBella, E.V., 2012. Spatiotemporal dictionary learning for undersampled dynamic MRI reconstruction via joint frame-based and dictionary-based sparsity. In: Biomedical Imaging (ISBI), 2012 9th IEEE International Symposium on. IEEE, pp. 318–321.
Blum, C., Roli, A., 2003. Metaheuristics in combinatorial optimization: overview and conceptual comparison. ACM Comput. Surv. (CSUR) 35 (3), 268–308.
Boyd, S., Parikh, N., Chu, E., Peleato, B., Eckstein, J., 2011. Distributed optimization and statistical learning via the alternating direction method of multipliers. Foundations and Trends® in Machine Learning 3 (1), 1–122.
Bristow, H., Eriksson, A., Lucey, S., 2013. Fast convolutional sparse coding. In: Proceedings of CVPR, pp. 391–398.
Caballero, J., Price, A.N., Rueckert, D., Hajnal, J.V., 2014. Dictionary learning and time sparsity for dynamic MR data reconstruction. IEEE Trans. Med. Imaging 33 (4), 979–994.
Caballero, J., Rueckert, D., Hajnal, J.V., 2012. Dictionary learning and time sparsity in dynamic MRI. In: Proceeding of MICCAI 2012. Springer, pp. 256–263.
CBIG, 2018. Computational Biomedical Imaging Group. https://research.engineering.uiowa.edu/cbig/content/matlab-codes-blind-compressed-sensing-bcs-dynamic-mri.
Chambolle, A., 2005. Total variation minimization and a class of binary MRF models. In: EMMCVPR, 5. Springer, pp. 136–152.
Chen, C., Li, Y., Axel, L., Huang, J., 2016. Real time dynamic MRI by exploiting spatial and temporal sparsity. Magn. Reson. Imaging 34 (4), 473–482.
Daubechies, I., 1992. Ten Lectures on Wavelets. SIAM.
Donoho, D.L., 2006. Compressed sensing. IEEE Trans. Inf. Theory 52 (4), 1289–1306.
El Khouli, R.H., Macura, K.J., Barker, P.B., Habba, M.R., Jacobs, M.A., Bluemke, D.A., 2009. Relationship of temporal resolution to diagnostic performance for dynamic contrast enhanced MRI of the breast. J. Magn. Reson. Imaging 30 (5), 999–1004. doi:10.1002/jmri.21947.
Goldstein, T., Osher, S., 2009. The split Bregman method for L1-regularized problems. SIAM J. Imaging Sci. 2 (2), 323–343.
Hoffmann, U., Brix, G., Knopp, M.V., Heß, T., Lorenz, W.J., 1995. Pharmacokinetic mapping of the breast: A new method for dynamic MR mammography. Magn. Reson. Med. 33 (4), 506–514. doi:10.1002/mrm.1910330408.
Jung, H., Sung, K., Nayak, K.S., Kim, E.Y., Ye, J.C., 2009. *k-t* FOCUSS: a general compressed sensing framework for high resolution dynamic MRI. Magn. Reson. Med. 61 (1), 103–116.
Jung, H., Ye, J.C., Kim, E.Y., 2007. Improved k–t blast and k–t sense using focuss. Phys. Med. Biol. 52 (11), 3201.
Kaggle, 2015. Data science bowl cardiac challenge data. https://www.kaggle.com/c/second-annual-data-science-bowl/data.
Lingala, S.G., Jacob, M., 2013. Blind compressive sensing dynamic MRI. IEEE Trans. Med. Imaging 32 (6), 1132–1145.
Luke, S., 2009. Essentials of Metaheuristics, 113. Lulu Raleigh.
Lustig, M., Donoho, D.L., Santos, J.M., Pauly, J.M., 2008. Compressed sensing MRI. IEEE Signal Process. Mag. 25 (2), 72–82.
Lustig, M., Santos, J.M., Donoho, D.L., Pauly, J.M., 2006. $k-t$ SPARSE: High frame rate dynamic MRI exploiting spatio-temporal sparsity. In: Proceedings of the 13th Annual Meeting of ISMRM, Seattle, 2420.
Ma, S., Yin, W., Zhang, Y., Chakraborty, A., 2008. An efficient algorithm for compressed MR imaging using total variation and wavelets. In: Computer Vision and Pattern Recognition, 2008. CVPR 2008. IEEE Conference on. IEEE, pp. 1–8.
Miao, X., Lingala, S.G., Guo, Y., Jao, T., Nayak, K.S., 2015. Accelerated cardiac cine using locally low rank and total variation constraints. In: Proceedings of the 23rd Annual Meeting, Toronto, Canada, p. 571.
Montefusco, L.B., Lazzaro, D., Papi, S., Guerrini, C., 2011. A fast compressed sensing approach to 3D MR image reconstruction. IEEE Trans. Med. Imaging 30 (5), 1064–1075.
Mühlenbein, H., Schomisch, M., Born, J., 1991. The parallel genetic algorithm as function optimizer. Parallel Comput. 17 (6–7), 619–632.
Nguyen-Duc, T., Jeong, W.-K., 2018. Compressed sensing dynamic MRI reconstruction using multi-scale 3D convolutional sparse coding with elastic net regularization. In: Biomedical Imaging (ISBI 2018), 2018 IEEE 15th International Symposium on. IEEE, pp. 332–335.
Otazo, R., Feng, L., Chandarana, H., Block, T., Axel, L., Sodickson, D.K., 2012. Combination of compressed sensing and parallel imaging for highly-accelerated dynamic MRI. In: Proceedings - International Symposium on Biomedical Imaging arXiv:NIHMS150003, pp. 980–983. doi:10.1109/ISBI.2012.6235721.
Otazo, R., Kim, D., Axel, L., Sodickson, D.K., 2010. Combination of compressed sensing and parallel imaging for highly accelerated first-pass cardiac perfusion MRI. Magn. Reson. Med. 64 (3), 767–776.
Quan, T.M., Han, S., Cho, H., Jeong, W.-K., 2015. Multi-GPU reconstruction of dynamic compressed sensing MRI. In: Proceeding of ISBI 2016. Springer, pp. 484–492.

Quan, T.M., Jeong, W.-K., 2016. Compressed sensing dynamic MRI reconstruction using GPU-accelerated 3D convolutional sparse coding. In: Proceeding of MICCAI, pp. 484–492.
Quan, T.M., Jeong, W.-K., 2016. Compressed sensing reconstruction of dynamic contrast enhanced MRI using GPU-accelerated convolutional sparse coding. In: Proceeding of ISBI 2016. IEEE, pp. 518–521.
Ravishankar, S., Bresler, Y., 2011. MR image reconstruction from highly undersampled k-space data by dictionary learning. IEEE Trans. Med. Imaging 30 (5), 1028–1041.
Ravishankar, S., Moore, B.E., Nadakuditi, R.R., Fessler, J.A., 2017. Low-rank and adaptive sparse signal (LASSI) models for highly accelerated dynamic imaging. IEEE Trans. Med. Imaging 36 (5), 1116–1128.
Shannon, C.E., 1949. Communication in the presence of noise. Proc. IRE 37 (1), 10–21.
Trémoulhéac, B., Dikaios, N., Atkinson, D., Arridge, S.R., 2014. Dynamic MR image reconstruction–Separation from undersampled $(k - t)$-Space via low-Rank plus sparse prior. IEEE Trans. Med. Imaging 33 (8), 1689–1701.
Wohlberg, B., 2014. Efficient convolutional sparse coding. In: Proceeding of ICASSP, pp. 7173–7177.
Wohlberg, B., 2016. Efficient algorithms for convolutional sparse representations. IEEE Trans. Image Process. 25 (1), 301–315.
Wu, Y.-C., Du, H., Mei, W., 2016. Filter-based compressed sensing MRI reconstruction. Int. J. Imaging Syst. Technol. 26 (3), 173–178.
Yang, Y., Liu, F., Xu, W., Crozier, S., 2015. Compressed sensing MRI via two-stage reconstruction. IEEE Trans. Biomed. Eng. 62 (1), 110–118.
Yao, J., Xu, Z., Huang, X., Huang, J., 2015. Accelerated dynamic MRI reconstruction with total variation and nuclear norm regularization. In: Proceeding of MICCAI. Springer, pp. 635–642.
Yao, J., Xu, Z., Huang, X., Huang, J., 2018. An efficient algorithm for dynamic MRI using low-rank and total variation regularizations. Med. Image Anal. 44, 14–27.
Zhu, Z., Yao, J., Xu, Z., Huang, J., Zhang, B., 2018. A simple primal-dual algorithm for nuclear norm and total variation regularization. Neurocomputing 289, 1–12.
Zou, H., Hastie, T., 2005. Regularization and variable selection via the elastic net. J. R. Stat. Soc.B 67 (2), 301–320.